# Role played by electrons in the stress-strain curves of ideal crystalline solids

Margherita Marsili,* Elisa Damiani, Davide Dalle Ave, Gabriele Losi, and M. Clelia Righi†
*Department of Physics and Astronomy, University of Bologna, Viale Carlo Berti Pichat 6/2, 40127 Bologna, Italy*

(Received 4 August 2025; revised 2 March 2026; accepted 7 April 2026; published 7 May 2026)

The mechanical properties of a solid, which relate its deformation to external applied forces, are key factors in enabling or disabling the use of an otherwise optimal material in any application, strongly influencing also its service lifetime. Intrinsic crystal deformation mechanisms, investigated experimentally on single crystals with low dislocation densities, have been studied theoretically through atomistic simulations, mainly focusing on lattice-induced instabilities. Here, instead, we employ density functional theory and a thermodynamic analysis to probe and analyze the way in which the electronic charge of crystalline solids (Cu, Al and diamond) respond to uniaxial strain and affects their mechanical properties. Indeed, despite the very simple nature of our models, and in the presence of minimal atomic displacements, we find that the stress strain curves of Cu and Al deviate from a simple linear elastic behavior. Within a thermodynamics perspective, the features of such curves can be interpreted in terms of first- and second-order phase transitions, which originate from Van Hove singularities of the electronic density of states crossing the Fermi level and electron redistribution within the solid.

DOI: 10.1103/nb45-7js6

## I. INTRODUCTION

The mechanical response of a solid, its capability of resisting or accommodating applied strains or stresses through reversible or irreversible deformations, dictates the range of mechanical stimuli the solid is able to comply with, directly influencing all its possible applications. Whenever loads, external forces, are applied to solid objects, they will deform. In the elastic regime the object will return to its original shape and size after load removal, whereas the plastic regime is characterized by irreversible deformations. This macroscopic, mechanical behavior of materials is clearly visible in the so called stress-strain curves, widely used reference graphs in material science and manufacturing, where the stress within a material is plotted against the relative change in length (or volume), namely the strain, it is opposing to.

In a generic ideal stress-strain plot under compressive load, it is possible to identify the elastic region, where the curve follows a linear trend, and, beyond it, the yield point that traditionally marks the transition between the linear-elastic regime and the plastic one where irreversible atomic planes sliding begins [1]. While at the macroscopic and mesoscopic levels the fingerprint of this behavior is displayed by cracks, dislocations, deformation bands, folds, shear markings and finally phase transitions, [2,3], at the microscopic, atomistic, level it may be anticipated by different kinds of processes ultimately leading to instabilities [4]: phonon modes softening [5–8], bonds formation or destabilization [9,10]. Indeed pressure has been shown to alter the chemical properties of elements, even literally subverting the periodic table [11,12].

Although most materials have a polycristalline character for which it is the defect structure (grain boundaries, dislocations, slip planes) that forces the way in which they will deform, single crystals with low dislocation densities, for which elastic/plastic deformations are due to purely intrinsic crystal deformations, are the best playground to explore basic deformation mechanisms. And, besides experiments, it is in this limiting case of perfect crystals that microscopic atomistic simulations can play a role providing further mechanistic insights on the mechanical behavior of materials. But while most of the studies focus on the properties and on the response of the atomic lattice itself as the primary source of instability and deformation path [6–8,13,14], the role and what directly happens to the electronic charge distribution has seldomly been addressed.

Here, we employ density functional theory (DFT) to directly probe the response of the electronic degrees of freedom of crystalline solids to uniaxial strain and look at how it affects their mechanical response. To do this we focus on the behavior of crystalline Al, Cu, and diamond bulks. To be able to identify basic electronic mechanisms, disentangled as much as possible from the ionic degrees of freedom, we make use of minimal models made up of few atoms per unit cell and not presenting defects, impurities, or flaws. Despite the extremely simplified nature of our systems, the simulated stress-strain curves of the metals display the typical trend of the macroscopic stress-strain curves that feature elastic to plastic regime transition. Moreover, our result show that the changes in the mechanical response of the solid, associated to the deviation from the linear behavior of the stress-strain curve, correspond to minimal deviations form the ideal geometry. Looking at the stress strain curve in a thermodynamics perspective, such critical points are signatures of crossovers, eventually leading to phase transition in the thermodynamic

*Contact author: margherita.marsili@unibo.it
†Contact author: clelia.righi@unibo.it

limit. We thus try to interpret such crossovers in terms of changes in the electronic structure. Our analysis show how the critical points of the stress-strain curve, are linked to changes in the amount of charge that is rearranged within and between the atomic planes upon loading. To gain further insights on the more complex case of Al, the evolution of the band structure and of the density of states (DOS) with load is analyzed. All the critical points of Al stress strain curve can be associated to Lifshitz transition in which stationary points of the band structure are crossing the Fermi level. However, while the DOS at the Fermi level is continuous at the critical strain associated to second-order crossovers, it display a discontinuity between 6% and 9% strain when a Van Hove singularity crosses the Fermi level, causing a first-order phase transition crossover.

The paper is organized as follows: after that computational details are presented, the stress-strain behavior of the three solids will be analyzed; then such stress-strain curves will be interpreted in a thermodynamics perspective and critical points linked to first and second-order crossovers will be identified; finally the physical origin of such criticalities will be explored linking the critical points present in the stress-strain curves to changes in electronic charge distribution within and between atomic planes, and to Van Hove singularities crossing the Fermi level.

## II. COMPUTATIONAL DETAILS

DFT calculations have been carried out as implemented in the quantum expresso package [15,16] using ultrasoft pseudopotential [17] and plane waves expansion. For the exchange-correlation functional, the Perdew-Burke-Ernzerhof [18] was chosen, adopting the parametrization by Rabe-Rappe-Kaxiras-Joannopoulos [19]. $18 \times 18 \times 18$, $12 \times 12 \times 12$, and $16 \times 16 \times 16$ Monkhorst-Pack grids were used to sample the Brillouin zone for Al, Cu, and diamond, respectively. The kinetic energy cutoff of 40 Ry (90 Ry), for the wave functions, and 320 Ry (720 Ry), for the charge density were employed for aluminum and diamond (copper). Forces were minimized employing variable cell calculations, optimizing at the same time both atomic positions and cell edges. The three bulk materials are simulated as cubic cells with the $xy$ plane parallel to the crystallographic (001) direction. For Al DOS calculations a $121 \times 121 \times 121$ k-point grid was used, employing the tetrahedron method to better describe Van Hove singularities. To simulate the effect of load, we strained the cells of the three materials along the z direction performing an accurate planar relaxation (xy cartesian plane) of the cell structures while allowing a full relaxation in all directions of the atomic positions. The remaining uniaxial stress along the vertical axis is derived from the DFT final stress tensor.

## III. STRESS-STRAIN BEHAVIOUR

Pressure is applied to the solids by reducing the bulk cells dimension along the z direction at the same time allowing the cell to deform within the xy plane, and all the atoms to fully relax. The cell dimension along $z$, $l$, was varied, by applying vertical strains $\epsilon_z = \frac{l-l_0}{l_0}$ ranging from $-0.01$ to $-0.09$ ($l_0$ being the equilibrium value). The details of the structural modifications of the three solids, such as area, volume changes, and deviations from ideal atomic positions are reported in the Supplemental Material (SM) [20], see also Refs. [21–25] therein.

Importantly, despite the fact that full relaxation is allowed, concerning the atomic positions no significant displacement is found at any strain even for the two metals. As reported in the SM [20], structural distortions and symmetry breaking analysis further confirmed that, as expected under uniaxial loading, the lattice exhibits a uniform tetragonal metric distortion, and that all atoms remain on a single crystallographic site (one equivalence class).

After constraining the unit cell dimension along the z direction to progressively compressed values and having allowed the full optimization of the cell in the xy plane, $\sigma_{zz}$ is the only nonnull element left in the stress tensor of the crystal. By collecting $\sigma_{zz}$ for increasing strains $\epsilon_z$, the stress-strain curves for the three materials, shown in Fig. 1, are built.

The stress-strain curves of the three materials differ qualitatively: while, within diamond, stress grows linearly in the whole strain range, in the case of Cu it grows fairly linearly up to 3%-4% strain, slightly lowering its slope between 0.01 and 0.02 strain, however at 0.03 strain it starts bending in a fashion that resembles a macroscopic elastic-plastic transition, where, beyond the yield point, the same increase of strain generates a lower increase of stress in the material: a sort of material softening. The case of Al presents an even more complex behavior: stress grows linearly up to $\sim$3% strain, from that point and up to $\sim$5.5% strain, stress is still increasing linearly but with a higher slope, as if the material were hardening. The curve then becomes nearly flat up to $\sim$7%, when it starts again to grow linearly.

The diamond stress-strain curve very well compares with that computed for uniaxial strain along the (001) direction in Ref. [26]. Interestingly, in experiments, Aluminum presents an extremely early onset of nonlinear elastic behavior and the yield point is difficult to identify. Indeed, experimental stress-strain curves of Al single crystals [27–32] show a bending behavior with decreasing slope already in the region close to 0 strain. Additional strain calculations from 0–1% in 0.1% steps are reported in the SM [20]. They show a linear elastic response with no discernible early nonlinearity, this is likely due to the idealized, defect-free model. Importantly in some of the curves [27,29], between $\sim$2% and $\sim$4% strain, a sudden increase of the slope of the stress-strain curve is also found, whereas other studies [28,32] show the hardening of the crystal following a region where the response is flat.

From the knowledge of the stress-strain curves and of the structural deformation of the three materials, their elastic properties, namely their Young's modulus and Poisson ratio, can be obtained. In all cases they compare well with experiments as shown in Table I (further details can be found in the SM [20]).

## IV. CRITICAL POINTS THERMODYNAMIC ANALYSIS

To gain insight and differentiate the critical points present in the stress-strain curve it is possible to take a thermodynamic perspective: in our simulations, at fixed 0 K temperature, the bulk cell is strained on the $z$ direction (by fixing the cell parameter $l_z$), allowing the basis area $A$ to vary in order to

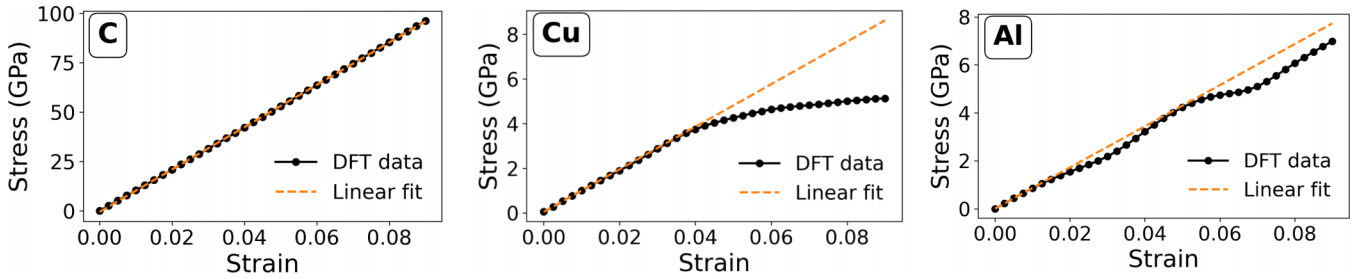


FIG. 1. Stress-strain curve for diamond (left), copper (center), aluminum (right). The linear regions are fitted with linear regression. Young's moduli are calculated as $E = \sigma_{zz}/\epsilon_z$ in the linear region. $\sigma_{zz}$ is the stress associated to the uniaxial strain along the z direction. (See SM [20]).

minimize the total energy. As a result the system is left with an internal pressure $P$ that originates from the internal forces that would restore the equilibrium geometry. The thermodynamic potential of choice is then the Helmholtz free energy, $F(T, l_z) = U - TS$, where the thermodynamic variable conjugated to $l_z$ is the total force acting along the $z$ direction $f_z = PA$ that keeps the strained system at equilibrium [33]. The differential of this thermodynamic potential would then be $dF = -SdT - f_z \cdot l_z = -SdT - pAdl_z$, its first-order derivative at fixed temperature $(\frac{\partial F}{\partial l_z})_T = -pA$, and its second-order derivative

$$\left(\frac{\partial^2 F}{\partial l_z^2}\right)_T = -A\left(\frac{\partial P}{\partial l_z}\right)_T - p\left(\frac{\partial A}{\partial l_z}\right)_T = T_1 + T_2. \quad (1)$$

$T_1 = -A(\frac{\partial P}{\partial l_z})_T$ represents the contribution to $(\frac{\partial^2 F}{\partial l_z^2})_T$ of the variation of pressure with respect to $l_z$, whereas $T_2 = -p(\frac{\partial A}{\partial l_z})_T$ is the contribution coming from the variation of the basis area.

The Helmholtz free energy, and its first and second-order derivatives with respect to strain are shown for diamond, together with the stress-strain curve, in Fig. 2(a), all three quantities are smoothly varying with strain, reflecting the unperturbed linear behavior of the entire stress-strain curve. In Fig. 2(b), the same quantities are shown for Cu. The Helmholtz free energy, which at $T = 0$ is nothing but the total energy of the system, shown in the top panel of Fig. 2(b), is continuous; its first derivative, second panel, resembles closely the stress-strain curve, implying that the basis area $A$ is a smooth function of $l_z$. The second-order derivative of the thermodynamic potential, shown in the bottom panel of Fig. 2(b), presents a discontinuity, corresponding to the point where the stress-strain curve (and $(\frac{\partial F}{\partial l_z})_T$) bends. Looking at the light blue dots of the same figure, it is clear how the discontinuity in $(\frac{\partial^2 F}{\partial l_z^2})_T$ arises from the term $T_1$, i.e., from an abrupt change in the slope of the pressure, in agreement with the behavior of the stress-strain curve.

TABLE I. Comparison between calculated and experimental values of Young's modulus $E$ and Poisson's ratio $\nu$ for Al, Cu, C. Experimental values are obtained from Ref. [1].

| Material | $E$ (GPa) | $E_{\text{expt}}$ (GPa) | $\nu$ | $\nu_{\text{expt}}$ |
|---|---|---|---|---|
| C | 1068 | 700–1200 | 0.107 | 0.10–0.30 |
| Cu | 97 | 110 | 0.341 | 0.34 |
| Al | 82 | 69 | 0.326 | 0.33 |

In the case of Al, shown in Fig. 2(c), the situation is more complex, as anticipated by the behavior of the stress-strain curve. Like in the case of Cu, the first derivative of the thermodynamic potential $(\frac{\partial F}{\partial l_z})_T$ (displayed in the central panel) closely resembles the stress-strain curve and, when further differentiating the thermodynamic potential, the main contribution arises from the variation of pressure with respect to $l_z$. However in this case we are in the presence of an oscillating behavior: around $\epsilon_z \sim 0.03$, where the stress-strain curve changes its slope, the $(\frac{\partial^2 F}{\partial l_z^2})_T$ has a sudden jump, a discontinuity similar to the one present for Cu, but in the opposite direction, i.e., increasing the value of $(\frac{\partial^2 F}{\partial l_z^2})_T$; subsequently, by applying further strain, $(\frac{\partial^2 F}{\partial l_z^2})_T$ immediately and quickly starts to decrease reaching an absolute minimum at $\epsilon_z \sim 0.0625$, within the region where the stress-strain curve becomes flat. The way in which the critical point locations are identified is detailed in the SM [20].

The thermodynamics perspective allows a better characterization and classification of the critical points of the stress-strain curves: the critical point of Cu manifests itself as a discontinuity in the second-order derivative of the thermodynamic potential, it can thus be classified as a crossover linked to a second-order phase transition happening at the bending points of the stress-strain diagram (and of the Poisson's ratio one, see SM [20]). In the case of Al we are instead in the presence of two different kind of critical points/regions. Around 3% strain, the discontinuity of $(\frac{\partial^2 F}{\partial l_z^2})_T$ can be associated to a crossover, eventually leading to second-order phase transition in the thermodynamic limit, consistent with what is happening for Cu, but in the opposite direction. The region around 6% strain instead looks more similar to a crossover leading, in the thermodynamic limit, to a first-order phase transition: the $pA$ plot [central panel of Fig. 2(c)] shows that, while varying the thermodynamic variable $l_z$ its conjugate variable $pA$ is nearly constant. A similar behavior is found in text books concerning the isothermal compression of a gas below its critical temperature, in this case, during the crossover, as the volume is reduced, pressure stays constant until all the vapor has condensed.

To further confirm this intepretation, in addition to the total energy (i.e., the Helmholtz free energy at 0 K), the Gibbs

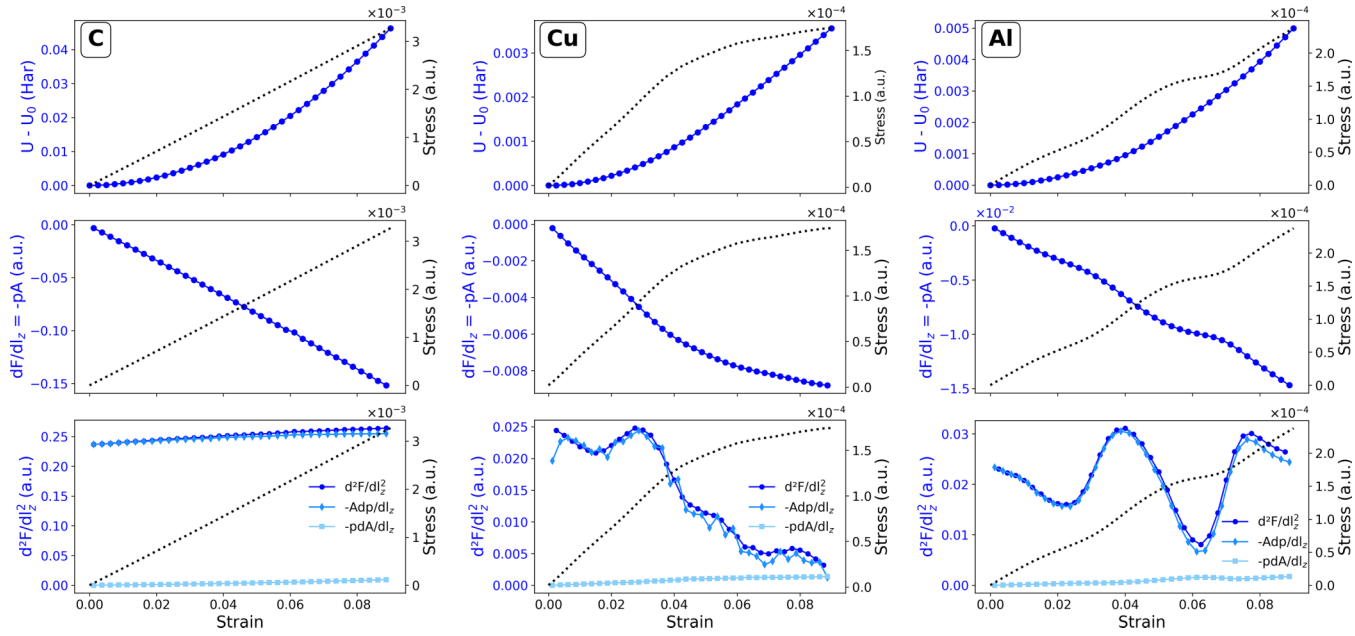


FIG. 2. (a) diamond; (b) Cu; (c) Al. From top to bottom: Helmholtz free energy $F$; its first-order derivative $(\frac{\partial F}{\partial l_z})$; $(\frac{\partial^2 F}{\partial l_z^2})_T = T_1 + T_2$, $T_1 = -A(\frac{\partial P}{\partial l_z})_T$ and $T_2 = -p(\frac{\partial A}{\partial l_z})_T$. In all panel stress values are reported as a black dotted line and refer to the right axis labels.

free energy is also considered. For uniaxial loads, the natural variable are the stress × area values conjugated to $l_z$. In the case of Al, the first-order derivative of the Gibbs free energy with respect to stress × area is continuous but changes slope at around 3% strain, whereas it appears to be discontinuous between 5% and 7% strain [Fig. 6(b) in the SM [20]]. The second-order derivative reflects these trends, displaying a discontinuity around 3% strain and a (negative) peak at 6% strain [Fig. 6(c) in the SM [20]].

Because phase transitions take place at nonanalytic points of the Gibbs free energy, in principle, no phase transition could occur within finite systems [33,34]. The presence of phase transitions in the thermodynamic potential derivatives should thus be carefully considered by extrapolating results to the thermodynamic limit. In general, as size increases, the nonanalytic behavior of thermodynamic quantities becomes more evident, for example jumps in the values of order parameters might become steeper. At the same time, while reaching the thermodynamic limit, the location of critical points might move in the space of thermodynamic parameters in a not trivial way, and this issue should also be carefully considered [35]. In plane wave codes simulations, employing periodic boundary conditions, results are converged with respect to k-point sampling of the Brillouin zone. Such sampling identifies the actual periodicity (and number) of the electronic wave functions (thus the system size from the electronic system perspective). Increasing the number of unit cells in our simulation and allowing the ionic position to relax could allow us to probe the effects of the lattice degrees of freedom on the stress-strain behavior of the solid. Nevertheless, this would overshade the effects of the electronic structure itself.

## V. ELECTRONIC CHARGE REDISTRIBUTION

The minimal nature of our models naturally quenches the lattice distortion degree of freedom. Indeed, as already mentioned, a symmetry analysis, performed with ase [36] and spglib [37] python libraries, reported in the SM [20], confirms that uniaxial loading produces only a uniform tetragonal metric distortion (change in $c/a$), with all atoms remaining symmetry-equivalent, and, moreover, the basis area is a smooth and a well-behaved function of $\epsilon_z$ (see SM [20]). Therefore the physical origin of the critical points in the stress strain curve, sign of first or second-order phase transitions, must be sought within the electronic system. We thus analyze the way the electronic charge redistributes itself upon increasing load. Indeed, charge redistribution has often been linked to many kind of phase transitions in the solid state: such as the structural phase transition of $CeO_2$ [38] and calcite [39], the antiferromagnetic phase transition of the SrFeAsF compound [40], and the isostructural phase transition in BiOCl [41]. And in general, trends in stress-strain behavior are often interpreted in terms of changes in bonding and the accompanying charge redistribution, which can be viewed both as a consequence and as a driving force of such bonding modifications: differences in charge redistribution explain the origin of an "easy" and "hard" direction within the $\{111\}\langle 112\rangle$ slip system of FCC Ni [42] and the higher shear strength of Al with respect to Cu [43], whereas the relationship between mechanical properties and electronic structure of Ag, Ir, and Al were investigated in terms of evolution with increasing shear strain of charge density critical points [44]. Moreover, a whole body of literature analyzing the mechanical response

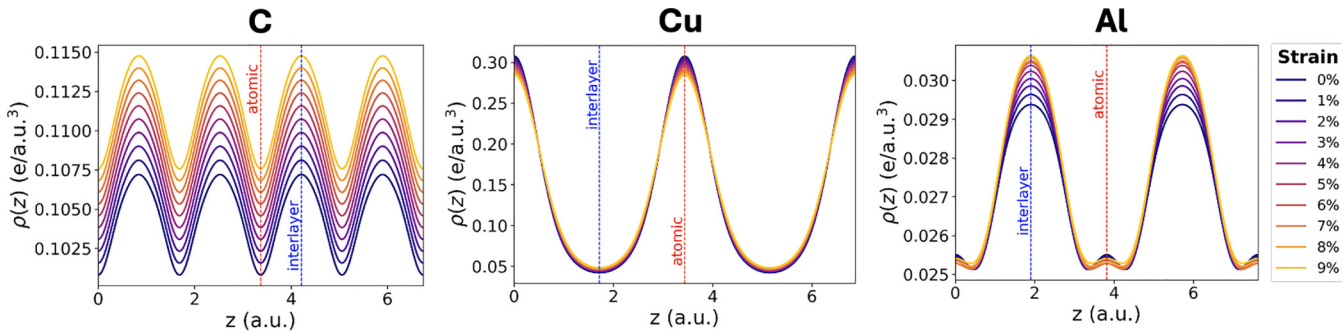


FIG. 3. C (left), Cu (center), and Al (right) charge density $\rho$ planar average profiles along the [001] direction for selected strain values. The position of an atomic plane is shown by a red-dashed line, whereas a middle position between two atomic planes is shown by a blue-dashed line.

upon concomitant shear and compression of light-elements transition-metal (TM) compounds such as TM-borides, carbides, and nitrides, reports that changes in bonding and charge redistribution are the key factors that ultimately determine the material strength [45–48]. Most of these studies employ complex unit cells and attain large strain values so that the most prominent stress-strain curves features are both concomitant to significant lattice distortions and to electronic charge rearrangements. In our case, the limited strain range (up to 1%) and cell size restrict the bond distance variations and lattice distortions so that the effects on the stress-strain curve are purely electronic.

Planar averages of charge density $\rho(z)$ are depicted in Fig. 3 as line profiles along the [001] direction. The position of atomic planes and interlayer planes are shown for all the slabs by red and blue dashed lines, respectively. The out-of-plane coordinates $z$ of strained cells were mapped onto that of the original, unstrained lattice by rescaling $z \mapsto z\,c_0/c$, with $c$ being the relaxed out-of-plane lattice parameter at a given strain and $c_0$ that at zero strain. By comparing the charge densities profiles of the three materials at equilibrium (corresponding to the $\epsilon_z = 0$ lines in Fig. 3), a main differences between aluminum and diamond on one side, and copper on the other is manifest: whereas charge peaks are found between atomic planes for aluminum and diamond, in the case where copper charge maxima are located at the atomic planes. When load is applied, charge density at the atomic planes of Al does not vary significantly whereas the excess charge, due to compression, is accumulated between atomic planes. On the other hand in Cu, there is a depletion of charge at the atomic planes and correspondingly a slight accumulation of charge between planes. Diamond apparently has a completely different behavior: in its case the overall charge profile is rising. However, by removing the contribution of the average density $\bar{\rho} = N_{\rm el}/V$, $V$ being the volume of the supercell, it is clear that, just like Al, diamond is slightly accumulating charge between atomic planes as shown in Fig. 4.

To spot possible peculiar behavior of the electronic charge at the critical points, modifications of the charge profiles are monitored at each strain increment, i.e., upon going from $\epsilon_z^{i-1}$ to $\epsilon_z^i$, being $\epsilon_z^0 = 0.0025$ and $\epsilon_z^{i_{MAX}} = 0.09$. Namely we compute the charge profile increments: $\Delta\rho(z, (\epsilon_z^i + \epsilon_z^{(i-1)})/2) = \rho(z, \epsilon_z^i) - \rho(z, \epsilon_z^{(i-1)})$.

Charge profiles increments, $\Delta\rho(z, \epsilon)$, are shown Fig. 5(b) for the case of diamond. In this case, both at the atomic planes and interlayer planes charge is increasing almost linearly with strain, as shown in the top two panels of the Fig. 5(c). The corresponding local charge increments, bottom two panels, are always positive and slightly constantly decreasing, as also attested by the "fading" heatmap [Fig. 5(a)].

The results for Cu are collected in Fig. 6. At the atomic planes charge is decreasing piece wise linearly with strain [top panel of Fig. 6(c)]. At the same time, at the interlayer planes, the electronic charge is linearly increasing [second top panel of Fig. 6(c)]. Consistently, charge increments within the interlayer planes (bottom panel) are nearly constant, whereas, within the atomic planes, (second bottom plot), $\Delta\rho(z_{\rm at}, (\epsilon_z))$ abruptly drops from $\sim -5.5 \times 10^{-4} e/\text{a.u.}^3$ to $\sim -7 \times 10^{-4} e/\text{a.u.}^3$ between 3% and 4% strain, signaling an increase of charge depletion rate (with strain) in that region. Remarkably, the drop in $\Delta\rho(z_{\rm at}, (\epsilon_z))$ is accompanied by the softening in the material, as shown by the stress-strain curve plotted for reference in red in the same figure. The discontinuous change of the rate of charge depletion at the atomic plane is thus marking the second-order phase transition identified at $\epsilon_z = 3\%$ in the thermodynamics analysis.

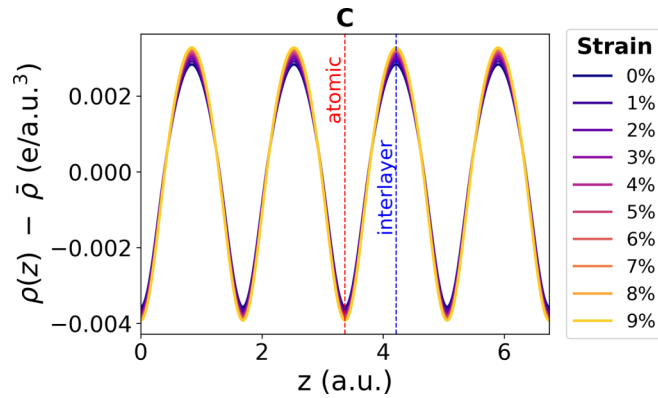


FIG. 4. Diamond charge density $\rho$ planar average profiles along the [001] direction shifted by $\bar{\rho} = N_{\rm el}/V$. An atomic plane and an interlayer plane are marked by red and blue dashed lines, respectively. $N_{\rm el}$ is the number of electrons of the supercell, while $V$ is the supercell volume.

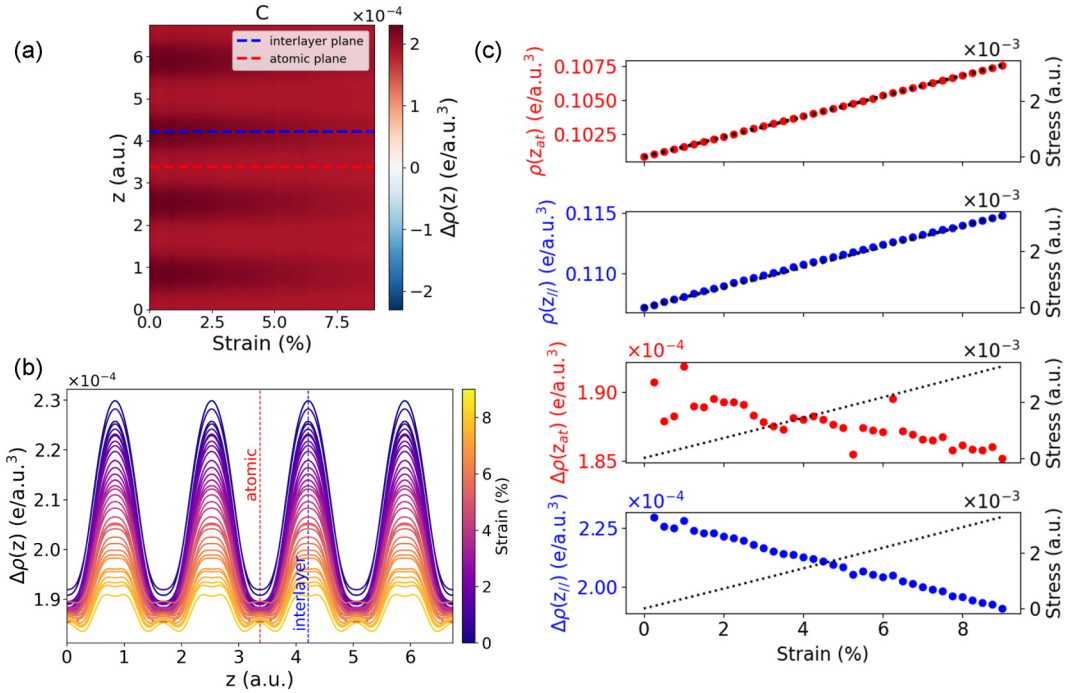


FIG. 5. (a) Charge profile increments $\Delta\rho(z, \epsilon_z)$ as a function of strain $\epsilon_z$ in the horizontal axis, and $z$ in the vertical axis. The positions of an interlayer and an atomic plane are marked by a dashed blue and red line, respectively. (b) Charge profile increments $\Delta\rho(z, \epsilon_z)$ as a function of $z$ for all the computed strain values. (c) From top to bottom: planar average charge densities profiles computed at atomic planes $\rho(z_{\text{at}}, \epsilon)$; values of the planar average charge densities profile computed at interlayer planes $\rho(z_{\parallel}, \epsilon)$; charge profile increments computed at atomic planes, i.e., cut of the heatmap (a) along the red-dashed line; charge profile increments computed at interlayer planes, i.e., cut of the heatmap (a) along the blue-dashed line. All panels refer to diamond.

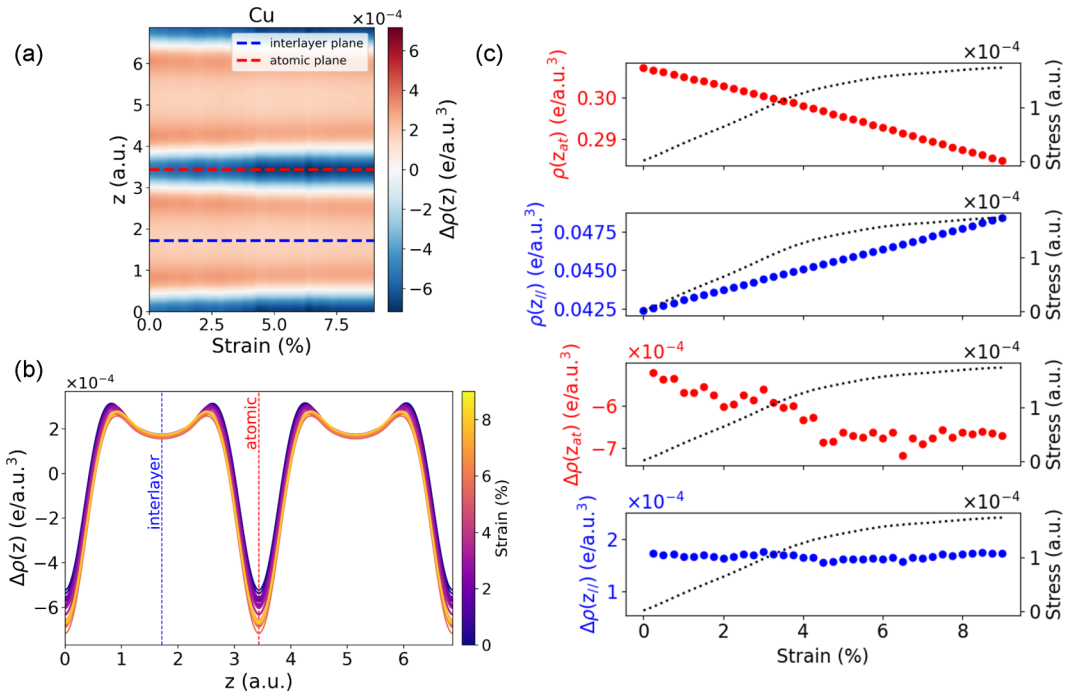


FIG. 6. (a) Charge profile increments $\Delta\rho(z, \epsilon_z)$ as a function of strain $\epsilon_z$ in the horizontal axis, and $z$ in the vertical axis. The positions of an interlayer and an atomic plane are marked by a dashed blue and red line, respectively. (b) Charge profile increments $\Delta\rho(z, \epsilon_z)$ as a function of $z$ for all the computed strain values. (c) From top to bottom: planar average charge densities profiles computed at atomic planes $\rho(z_{\text{at}}, \epsilon)$; values of the planar average charge densities profile computed at interlayer planes $\rho(z_{\parallel}, \epsilon)$; charge profile increments computed at atomic planes, i.e., cut of the heatmap (a) along the red-dashed line; charge profile increments computed at interlayer planes, i.e., cut of the heatmap (a) along the blue-dashed line. All panels refer to Cu.

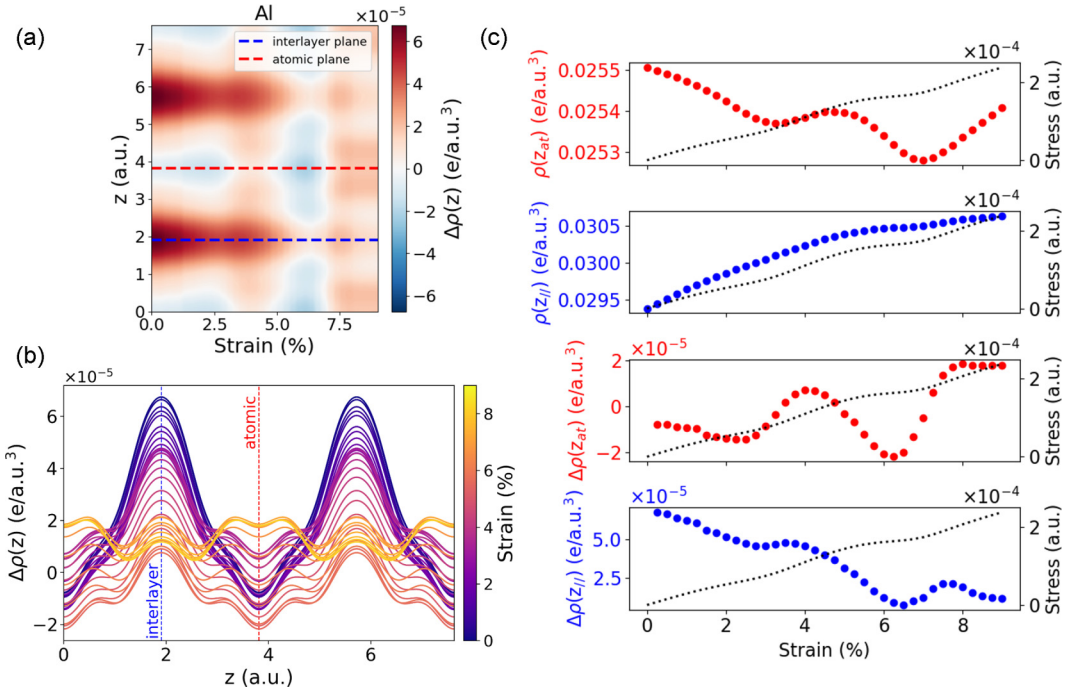


FIG. 7. (a) Charge profile increments $\Delta\rho(z, \epsilon_z)$ as a function of strain $\epsilon_z$ in the horizontal axis, and $z$ in the vertical axis. The positions of an interlayer and an atomic plane are marked by a dashed blue and red line, respectively. (b) Charge profile increments $\Delta\rho(z, \epsilon_z)$ as a function of $z$ for all the computed strain values. (c) From top to bottom: planar average charge densities profiles computed at atomic planes $\rho(z_{\rm at}, \epsilon)$; values of the planar average charge densities profile computed at interlayer planes $\rho(z_\parallel, \epsilon)$; charge profile increments computed at atomic planes, i.e., cut of the heatmap (a) along the red-dashed line; charge profile increments computed at interlayer planes, i.e., cut of the heatmap (a) along the blue-dashed line. All panels refer to Al.

The complexity of Al stress-strain curve is reflected also in the evolution of its charge profiles and of the charge increments, collected in Fig. 7. Within the interlayer planes [Fig. 7(c), second panel from the top], charge consistently grows in the entire strain range with changes in slope that reflect those of the stress-strain curve. In contrast, at the atomic planes the, overall decreasing, charge features oscillations that clearly follow those of the second derivative of the thermodynamic potential [bottom panel of Fig. 2(c)]. Looking at the charge increments at the two critical points in the two bottom panels of Fig. 7(c), we see that the second-order phase transition crossover at $\epsilon_z = 0.03$ is characterized by a discontinuity of the charge increments at the atomic plane and nearly constant increments at the interlayer planes, resembling the situation of Cu. It is interesting to note that the sign of the discontinuity correlates with the mechanical behavior: in the Cu case, there is a negative jump of the increments and the material is softening, whereas in Al there is a positive jump and the material hardens. The first-order phase transition crossover at $\epsilon_z \sim 6\%$ is instead marked by a deep minimum of both the local charge increments. The pronounced minima in the local charge increments at $\epsilon_z \sim 6\%$ in Al, together with the oscillatory trend of $\rho_{\rm at}$ [Fig. 7(c), top panel], can be interpreted by analyzing the strain-induced evolution of the band structure, discussed in the next Section.

## VI. AL ELECTRONIC STRUCTURE EVOLUTION WITH STRAIN

Materials band structures can be profoundly altered by pressure, and when new bands begin crossing the Fermi level, or bands previously crossing it are entirely pushed below or above it, the Fermi surface changes its topology, a phenomenon known as Lifshitz transition [49]. Lifshitz transitions are accompanied by all sorts of anomalies in solids regarding phonon frequencies, resistivity, and mechanical properties [50–52]. Importantly, in the case of Al under hydrostatic pressure, a Lifhsitz transition was detected by nuclear magnetic resonance [53]; we have thus analyzed the evolution of its electronic DOS and band structure with increasing uniaxial load.

Figure 8(a) shows the evolution of Al DOS for energies close to the Fermi level, marked by a dashed black line, for strain values between 4.5% and 9.0%. A minimum of the DOS can be clearly seen crossing the Fermi level between 5.5% and 6.5% strain. The DOS profiles for selected strains, Fig. 8(b) show this feature, which is due to both a contribution due to $s$ electrons [Fig. 8(c)] and $p$ electrons [Fig. 8(d)]. Importantly, as shown in the SM [20], around the critical point $\epsilon_z \sim 3\%$, the Al DOS close to the Fermi level does not display any significant change. In addition, in Fig. 8 (SM) [20] the evolutions of the Fermi level and that of the DOS at the Fermi

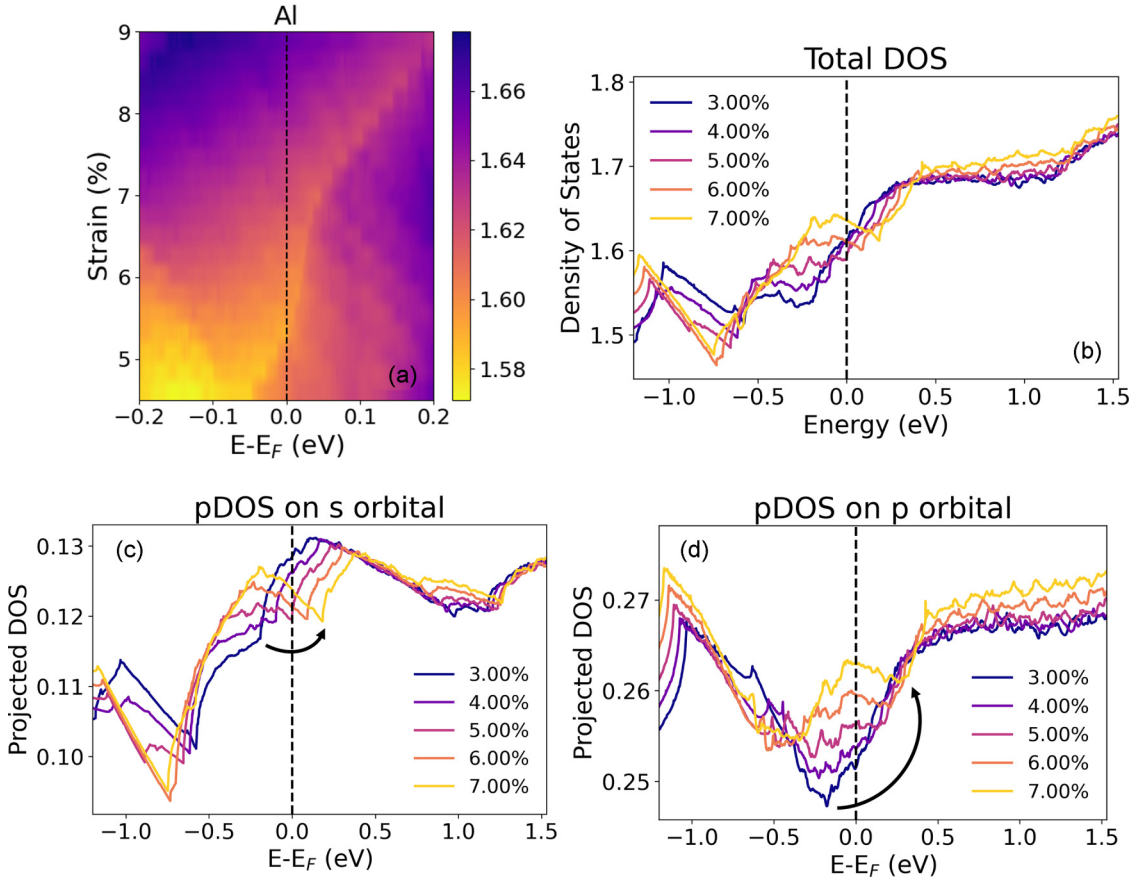


FIG. 8. (a) Al DOS close to the Fermi level for strain values beteween 4.5% and 9.0%. (b) Al total DOS for selected strain value around the critical value of $\epsilon_z = 0.06$. (c) Al DOS projected on the s orbitals for selected strain value around the critical value of $\epsilon_z = 0.06$. (d) Al DOS projected on the p orbitals for selected strain value around the critical value of $\epsilon_z = 0.06$.

level with strain for the case of Al are shown. At around 3% strain, there is a change in slope in the Fermi level, Whereas ∼6% strain is between a high/low Fermi level [or a low/high DOS($E_F$)] regimes.

It can be thus concluded that the first-order critical point around $\epsilon_z \sim 6\%$ in Al is linked to Van Hove singularities crossing the Fermi level and altering the availability of electronic states for the response of the solid to pressure. Indeed, the flattening of the Al stress-strain curve around ∼6% strain closely reminds one of the giant softening of the $Sr_2RuO_4$ lattice associated with a Lifshitz transition characterized by a Van Hove singularity crossing the Fermi level [52].

To explain the oscillatory behavior of the charge at the atomic plane in Al and to further confirm the presence of Lifshitz transitions, the evolution of the band structure with increasing strain was monitored, focusing on a narrow energy window around the Fermi level $E_F$. In Fig. 9, we report the band structure along the Γ-X-P high-symmetry path. Band structures plotted along the complete $X_1$-Z-Γ-X-P k path adapted from Ref. [7] are reported in the SM [20]. In Fig. 9 the horizontal and vertical dashed lines mark the Fermi level and the X point, respectively.

Between 0 and 4% strain the most significant changes happen along the Γ-X path. At zero strain, bands are degenerate in the vicinity of X, the higher energy ones displaying a saddle point at X. Upon increasing $\epsilon_z$, the bands degeneracy progressively lifts for k points away from X, while symmetry keeps them degenerate at the X point throughout the entire load ramp. At $\epsilon_z \sim 2\%$ [Fig. 9(c)], the blue ($n = 7$)/green ($n = 6$) band displays two local minima/maxima on the Γ-X path ($n$ here refers to the band index). Upon increasing $\epsilon_z$, the higher-energy maximum (green) and minimum (blue) on the left side progressively cross $E_F$ becoming unoccupied and producing a loss of available states at the Fermi level. Importantly, at $\epsilon_z \sim 3\%$ [Fig. 9(d)], both extrema lie very close to $E_F$. The evolution of the charge density profiles of both $n = 6$ and $n = 7$ states are shown in Fig. 11 of the SM [20]: both states are localized on the atomic planes and keep this character upon crossing the Fermi level. Although the charge density of a single Kohn-Sham state does not determine the total charge density discussed in Sec. V this crossing might be associated to the local minimum of $\rho(z_{at})$ found around 3% strain for Al [see Fig. 7(c), top panel]. Therefore also the second-order critical point of the Al stress-strain curve might be interpreted in terms of a Lifhsitz transition. Indeed the change in slope of $l_z = \frac{dG}{d(pA)}$ (see the Gibbs free energy analysis in the SM [20]) is closely reminiscent of the change in slope of the pressure dependence of the volume of NbAs [50] and NbP [51] at a Lifshitz transition.

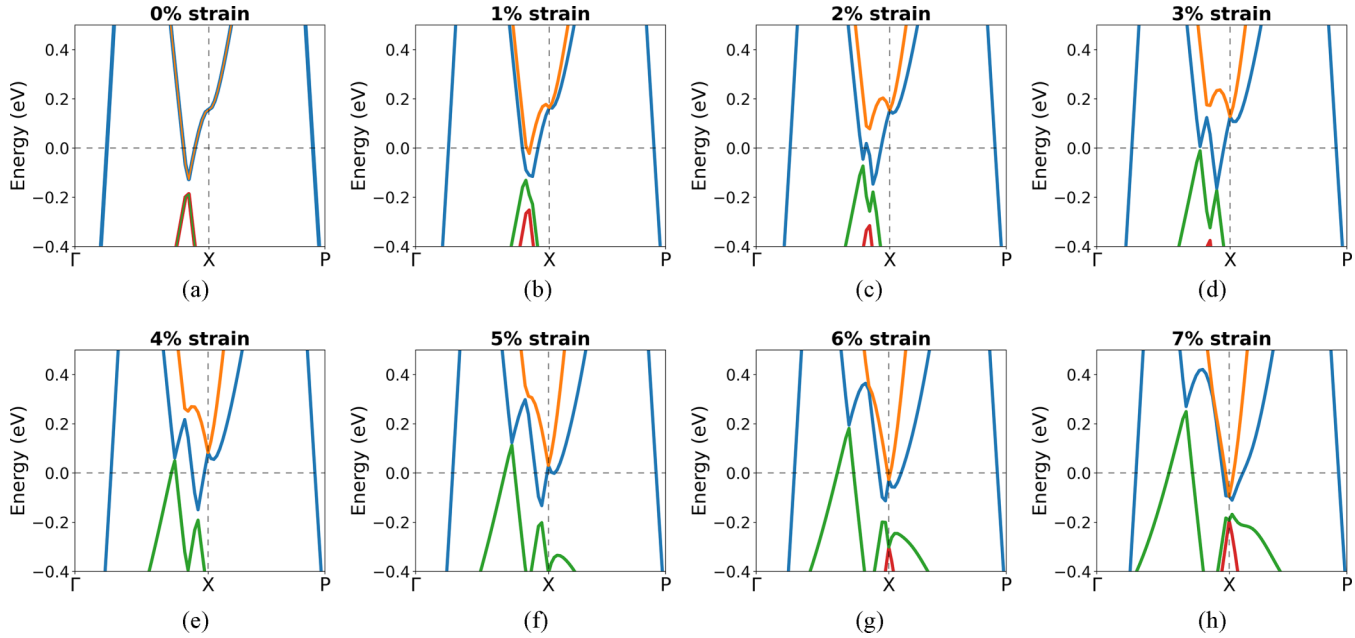


FIG. 9. Evolution of Al band structure upon strain along the Γ-X-P k path. The Fermi level is set at 0 and is marked by the horizontal dashed line. The vertical dashed line marks the X point.

For larger strains main changes arise along the X-P line. At $\epsilon_z \sim 5\%$ [Fig. 9(f)], both the $n = 7$ and $n = 8$ states at X and the minimum on the X-P side of the $n = 7$, blue band cross $E_F$ and become occupied. This marks a substantial rearrangement of the electronic structure, consistent with the changes observed in the DOS. A detailed analysis of the character of the states associated with the band extrema crossing the Fermi level also in this case is provided in the SM (Fig. 10) [20]. Remarkably, the states crossing $E_F$ at the X point around $\epsilon_z \sim 5\%$ undergo a clear change in character, shifting from atomic-plane localization to interlayer localization while going from unoccupied to occupied, explaining the second minimum in $\rho(z_{\text{at}})$ [see Fig. 7(c), top panel].

## VII. CONCLUSIONS

In conclusion we employed DFT to study the response of the electronic system of crystalline Al, Cu, and diamond to uniaxial strain. In order to quench lattice deformation degrees of freedom and focus on basic electronic mechanisms, we make use of minimal models made up of few atoms per unit cell and not presenting defects, impurities, or flaws. Young's moduli and Poisson ratio, computed in the limit of low strains, agree well with experimental values. Surprisingly, despite the very simple nature of our models, and in the presence of minimal atomic displacements, the stress strain curves of Cu and Al deviate from a simple linear elastic behavior.

Within a thermodynamic perspective two distinct features can be distinguished in the stress-strain curve of the two metals: in one case (at ∼4% strain for Cu and ∼3% strain for Al) the change in the slope of the stress-strain curve is a manifestation of the discontinuity of the second-order derivative of the thermodynamic potential. In the second case, happening in the region around ∼6% strain for Al, the stress-strain curve is almost flat, at same time the first-order derivative of the thermodynamic potential, the thermodynamic variable $pA$, conjugated to $l_z$, is substantially constant as $l_z$ varies, resembling crossover leading, in the thermodynamic limit, to a first-order phase transition. Besides providing a better classification and characterization of the critical points of the stress strain curve, the thermodynamics analysis confirms the fundamental role played by the charge depletion/accumulation at the atomic and interlayer planes. Indeed simple bending of the stress-strain curve, associated to the softening (for Cu) and hardening (for Al) of the materials, and linked to sudden decrease for Cu and increase for Al of $(\frac{\partial^2 F}{\partial l_z^2})_T$ —the rate of change with strain of $pA$, the force by which the unit cell of the crystal opposes to the compression — is accompanied by a sudden increase in atomic plane charge depletion for Cu and, vice versa, a sudden increase in atomic plane charge accumulation for Al. In the meanwhile, charge accumulation at the interlayer planes stays nearly constant.

The second kind of structure, where the stress-strain curve of Al is nearly flat, is a sort of extreme softening of the material; indeed, the increase of strain is not producing any change in $pA$, the force by which the solid is responding to the external stimulus. In this region, charge depletion at atomic planes is at it maximum, at the same time charge accumulation in the interlayer region also changes and is at its global minimum.

Both first and second-order critical points in Al stress-strain curve are associated to band structure stationary points crossing the Fermi level. Both kinds of critical points are thus interpretable as Lifshitz transitions. However, while first-order critical points are also associated with a discontinuity of the density of state at the Fermi level, such a quantity is continuous in the case of second-order crossovers. Indeed, since structural degrees of freedom are restricted in our minimal

model, stress-strain anomalies are linked to changes in the availability of electron relaxation channels that are consequence of band stationary points crossing the Fermi level with increasing load. The magnitude (and quality) of such changes affects the continuity/discontinuity of the way in which the system equilibrates the applied load, i.e., its mechanical response.

In realistic macroscopic situations many processes take place, such as gliding along crystallographic planes, formation of dislocations, deformation bands, folds etc., which conceal the microscopic response of the electronic system alone. Our findings unveil the specific way in which the electronic degrees of freedom might contribute to or actually cause the mechanical response of materials. The analysis of how the electronic charge within the solid is affected by mechanical stresses makes this study relevant also in the field of tribology. Indeed adhesion and frictional forces are dictated by the electronic charge redistribution occurring when two isolated surfaces are mated to form an interface [54].

## ACKNOWLEDGMENTS

M.M. thanks Prof. F. Zamponi and Dr. P. Restuccia for fruitful discussions. These results are part of the "Advancing Solid Interface and Lubricants by First Principles Material Design (SLIDE)" project that has received funding from the European Research Council (ERC) under the European Union's Horizon 2020 research and innovation program (Grant Agreement No. No. 865633). The authors acknowledge funding by the European Union - NextGenerationEU (National Sustainable Mobility Center CN00000023, Italian Ministry of University and Research Decree No. 1033 - 17/06/2022, Spoke 11 - Innovative Materials & Lightweighting) and by the European Union - NextGenerationEU (Spoke 6 - Mulstiscale Modelling & Engineering Applications). The opinions expressed are those of the authors only and should not be considered as representative of the European Union or the European Commission's official position. Neither the European Union nor the European Commission can be held responsible for them. Computational resources were provided by CINECA under the ISCRA initiative and by the CRESCO/ENEAGRID High Performance Computing infrastructure [55].

## DATA AVAILABILITY

The data that support the findings of this article are not publicly available upon publication because it is not technically feasible and/or the cost of preparing, depositing, and hosting the data would be prohibitive within the terms of this research project. The data are available from the authors upon reasonable request.

[1] W. Callister Jr. and D. Rethwisch, *Materials Science and Engineering: An Introduction*, 10th ed. (Wiley, New York, 2018).

[2] L. He, D. Polsin, S. Zhang, G. W. Collins, and N. Abdolrahim, Phase transformation path in aluminum under ramp compression; simulation and experimental study, Sci. Rep. **12**, 18954 (2022).

[3] I. V. Bespalova, L. A. Teplyakova, and T. S. Kunitsyna, Localization of plastic deformation in aluminum single crystals at different scale levels, Russian Phys. J. **60**, 502 (2017).

[4] K. Lion, P. Pavone, and C. Draxl, Elastic stability of $Ga_2O_3$: Addressing the $\beta$ to $\alpha$ phase transition from first principles, Phys. Rev. Mater. **6**, 013601 (2022).

[5] G. Grimvall, B. Magyari-Köpe, V. Ozoliņš, and K. A. Persson, Lattice instabilities in metallic elements, Rev. Mod. Phys. **84**, 945 (2012).

[6] S. M.-M. Dubois, G.-M. Rignanese, T. Pardoen, and J.-C. Charlier, Ideal strength of silicon: An *ab initio* study, Phys. Rev. B **74**, 235203 (2006).

[7] D. M. Clatterbuck, C. R. Krenn, M. L. Cohen, and J. W. Morris, Phonon instabilities and the ideal strength of aluminum, Phys. Rev. Lett. **91**, 135501 (2003).

[8] D. Roundy, C. R. Krenn, M. L. Cohen, and J. W. M. Jr., The ideal strength of tungsten, Philos. Mag. A **81**, 1725 (2001).

[9] C. Jiang and S. G. Srinivasan, Unexpected strain-stiffening in crystalline solids, Nature (London) **496**, 339 (2013).

[10] B. Li, Y. Ding, W. Yang, L. Wang, B. Zou, J. Shu, S. Sinogeikin, C. Park, G. Zou, and H. kwang Mao, Calcium with the $\beta$-tin structure at high pressure and low temperature, Proc. Natl. Acad. Sci. USA **109**, 16459 (2012).

[11] X. Dong, A. Oganov, H. Cui, X.-F. Zhou, and H.-T. Wang, Electronegativity and chemical hardness of elements under pressure, Proc. Natl. Acad. Sci. USA **119**, e2117416119 (2022).

[12] J. Hou, X. Wang, Q. Zhu, X. Shao, S. Qiu, X.-J. Weng, G. Yang, X. Dong, X.-F. Zhou, and Y. Tian, Chemical bonding between helium and fluorine under pressure, J. Am. Chem. Soc. **147**, 33453 (2025).

[13] B. H. Cogollo-Olivo, S. Biswas, S. Scandolo, and J. A. Montoya, Phase diagram of oxygen at extreme pressure and temperature conditions: An *ab initio* study, Phys. Rev. B **98**, 094103 (2018).

[14] C. Marini, D. Chermisi, M. Lavagnini, D. Di Castro, C. Petrillo, L. Degiorgi, S. Scandolo, and P. Postorino, High-pressure phases of crystalline tellurium: A combined Raman and *ab initio* study, Phys. Rev. B **86**, 064103 (2012).

[15] P. Giannozzi, S. Baroni, N. Bonini, M. Calandra, R. Car, C. Cavazzoni, D. Ceresoli, G. L. Chiarotti, M. Cococcioni, I. Dabo, A. D. Corso, S. de Gironcoli, S. Fabris, G. Fratesi, R. Gebauer, U. Gerstmann, C. Gougoussis, A. Kokalj, M. Lazzeri, L. Martin-Samos, *et al.*, Quantum espresso: A modular and open-source software project for quantum simulations of materials, J. Phys.: Condens. Matter **21**, 395502 (2009).

[16] P. Giannozzi, O. Andreussi, T. Brumme, O. Bunau, M. B. Nardelli, M. Calandra, R. Car, C. Cavazzoni, D. Ceresoli, M. Cococcioni, N. Colonna, I. Carnimeo, A. D. Corso, S. de Gironcoli, P. Delugas, R. A. DiStasio, A. Ferretti, A. Floris, G. Fratesi, G. Fugallo, *et al.*, Advanced capabilities for materials modelling with Quantum espresso, J. Phys.: Condens. Matter **29**, 465901 (2017).

[17] D. Vanderbilt, Soft self-consistent pseudopotentials in a generalized eigenvalue formalism, Phys. Rev. B **41**, 7892 (1990).

[18] J. P. Perdew, K. Burke, and M. Ernzerhof, Generalized gradient approximation made simple, Phys. Rev. Lett. **77**, 3865 (1996).

[19] A. M. Rappe, K. M. Rabe, E. Kaxiras, and J. D. Joannopoulos, Optimized pseudopotentials, Phys. Rev. B **41**, 1227 (1990).

[20] See Supplemental Material at http://link.aps.org/supplemental/10.1103/nb45-7js6 for details of the structural modifications of the three solids, Gibbs free energy (and its first and second-order derivatives) plots, structural distortions and symmetry breaking analysis, elastic properties, strain calculations from 0–1% in 0.1% steps for Al, critical point location identification procedure, Al DOS evolution around the critical point $\epsilon_z \sim 3\%$, evolutions of Al Fermi level and DOS at the Fermi level with strain, Al band structures plotted along the $X_1$-Z-Γ-X-P k path, evolution of charge density profiles related to relevant Kohn-Sham tates in Al, analysis of the character of the states associated with the band extrema crossing the Fermi level for Al.

[21] H. Hou, Z. Wen, Y. Zhao, L. Fu, N. Wang, and P. Han, First-principles investigations on structural, elastic, thermodynamic and electronic properties of $Ni_3X$ (X = Al, Ga and Ge) under pressure, Intermetallics **44**, 110 (2014).

[22] F. Nestola, G. Zaffiro, M. L. Mazzucchelli, P. Nimis, G. B. Andreozzi, B. Periotto, F. Princivalle, D. Lenaz, L. Secco, L. Pasqualetto, A. M. Logvinova, N. V. Sobolev, A. Lorenzetti, and J. W. Harris, Diamond-inclusion system recording old deep lithosphere conditions at Udachnaya (Siberia), Sci. Rep. **9**, 12586 (2019).

[23] G. N. Greaves, A. L. Greer, R. S. Lakes, and T. Rouxel, Poisson's ratio and modern materials, Nat. Mater. **10**, 823 (2011).

[24] E. Güler and M. Güler, High pressure elastic properties of wurtzite aluminum nitrate, Chin. J. Phys. **52**, 1625 (2014).

[25] E. Güler and M. Gueler, Elastic and mechanical properties of cubic diamond under pressure, Chin. J. Phys. **53**, 195 (2015).

[26] X. Luo, Z. Liu, B. Xu, D. Yu, Y. Tian, H.-T. Wang, and J. He, Compressive strength of diamond from first-principles calculation, J. Phys. Chem. C **114**, 17851 (2010).

[27] V. Romanova, R. Balokhonov, O. Zinovieva, D. Lychagin, E. Emelianova, and E. Dymnich, Mechanical aspects of non-homogeneous deformation of aluminum single crystals under compression along [100] and [110] directions, Metals **12**, 397 (2022).

[28] R. Becker, J. F. Butler, H. Hu, and L. A. Lalli, Analysis of an aluminum single crystal with unstable initial orientation (001) [110] in channel die compression, Metall. Trans. A **22**, 45 (1991).

[29] A. S. Khan, J. Liu, J. W. Yoon, and R. Nambori, Strain rate effect of high purity aluminum single crystals: Experiments and simulations, Int. J. Plast. **67**, 39 (2015).

[30] J. F. Bell and R. E. G. Jr., An experimental study of the double slip deformation hypothesis for face-centred cubic single crystals, Philos. Mag. **15**, 469 (1967).

[31] S. Ha and K. Kim, Heterogeneous deformation of Al single crystal: Experiments and finite element analysis, Math. Mech. Solids **16**, 652 (2011).

[32] F. Basson and J. Driver, Deformation banding mechanisms during plane strain compression of cube-oriented f.c.c. crystals, Acta Mater. **48**, 2101 (2000).

[33] S. J. Blundell and K. M. Blundell, *Concepts in Thermal Physics* (Oxford University Press, Oxford, 2009).

[34] C. J. Thomson, *Mathematical Statistical Mechanics* (Princeton University Press, Princeton, NJ, 1972).

[35] S. Rossi, G. Biroli, M. Ozawa, G. Tarjus, and F. Zamponi, Finite-disorder critical point in the yielding transition of elasto-plastic models, Phys. Rev. Lett. **129**, 228002 (2022).

[36] A. Hjorth Larsen, J. Jørgen Mortensen, J. Blomqvist, *et al.*, The atomic simulation environment—a python library for working with atoms, J. Phys.: Condens. Matter **29**, 273002 (2017).

[37] A. Togo, K. Shinohara, and I. Tanaka, Spglib: A software library for crystal symmetry search, Sci. Technol. Adv. Mater.: Methods **4**, 2384822 (2024).

[38] K.-W. Park and C. S. Kim, Deformation-induced charge redistribution in ceria thin film at room temperature, Acta Mater. **191**, 70 (2020).

[39] M. Stachowicz, A. A. Huć, T. Porębа, M. Mezouar, P. Dera, and K. Woźniak, Charge shift in calcite before high-pressure phase transition, J. Am. Chem. Soc. **148**, 6860 (2026).

[40] Z. Li, Y. Fang, X. Ma, H. Pang, and F. Li, Charge redistribution at the antiferromagnetic phase transition in the SrFeAsF compound, Phys. Rev. B **84**, 134509 (2011).

[41] J. Zhao, L. Xu, Y. Liu, Z. Yu, C. Li, Y. Wang, and Z. Liu, Isostructural phase transition in bismuth oxide chloride induced by redistribution of charge under high pressure, J. Phys. Chem. C **119**, 27657 (2015).

[42] Y.-L. Liu, Y. Zhang, H.-B. Zhou, G.-H. Lu, and M. Kohyama, Theoretical strength and charge redistribution of fcc Ni in tension and shear, J. Phys.: Condens. Matter **20**, 335216 (2008).

[43] S. Ogata, J. Li, and S. Yip, Ideal pure shear strength of aluminum and copper, Science **298**, 807 (2002).

[44] N. Kioussis, M. Herbranson, E. Collins, and M. E. Eberhart, Topology of electronic charge density and energetics of planar faults in fcc metals, Phys. Rev. Lett. **88**, 125501 (2002).

[45] H. Wu, H. Sun, and C. Chen, Unexpected structural softening of interstitial boron solid solution $WB_{3+x}$, Appl. Phys. Lett. **105**, 211901 (2014).

[46] C. Liu, X. Gao, K. Zhang, W. Zheng, and C. Chen, Exceptional strain strengthening and tuning of mechanical properties of TiN, Phys. Rev. B **106**, 054112 (2022).

[47] Z. Pan, H. Sun, and C. Chen, Colossal shear-strength enhancement of low-density cubic $BC_2N$ by nanoindentation, Phys. Rev. Lett. **98**, 135505 (2007).

[48] Q. Li, D. Zhou, W. Zheng, Y. Ma, and C. Chen, Anomalous stress response of ultrahard $WB_n$ compounds, Phys. Rev. Lett. **115**, 185502 (2015).

[49] I. M. Lifshitz, Anomalies of electron characteristics of a metal in the high pressure region, Z. Eksp. Teor. Fiz. **38**, 1569 (1960) [Sov. Phys. JETP **1130** (1960)].

[50] S. N. Gupta, A. Singh, K. Pal, D. V. Muthu, C. Shekhar, M. A. Elghazali, P. G. Naumov, S. A. Medvedev, C. Felser, U. V. Waghmare, and A. K. Sood, Pressure-induced Lifshitz and structural transitions in NbAs and TaAs: Experiments and theory, J. Phys.: Condens. Matter **30**, 185401 (2018).

[51] S. N. Gupta, A. Singh, K. Pal, D. V. S. Muthu, C. Shekhar, Y. Qi, P. G. Naumov, S. A. Medvedev, C. Felser, U. V. Waghmare, and A. K. Sood, Pressure-induced Lifshitz transition in NbP: Raman, X-ray diffraction, electrical transport, and density functional theory, Phys. Rev. B **97**, 064102 (2018).

[52] H. M. Noad, K. Ishida, Y. S. Li, E. Gati, V. Stangier, N. Kikugawa, D. A. Sokolov, M. Nicklas, B. Kim, I. I. Mazin, M. Garst, J. Schmalian, A. P. Mackenzie, and C. W. Hicks, Giant lattice softening at a Lifshitz transition in $Sr_2RuO_4$, Science **382**, 447 (2023).

[53] T. Meissner, S. K. Goh, J. Haase, M. Richter, K. Koepernik, and H. Eschrig, Nuclear magnetic resonance at up to 10.1 GPa pressure detects an electronic topological transition in aluminum metal, J. Phys.: Condens. Matter **26**, 015501 (2014).

[54] M. Wolloch, G. Levita, P. Restuccia, and M. C. Righi, Interfacial charge density and its connection to adhesion and frictional forces, Phys. Rev. Lett. **121**, 026804 (2018).

[55] F. Iannone, F. Ambrosino, G. Bracco, M. De Rosa, A. Funel, G. Guarnieri, S. Migliori, F. Palombi, G. Ponti, G. Santomauro, and P. Procacci, CRESCO ENEA HPC clusters a working example of a multifabric GPFS Spectrum Scale layout, in *2019 International Conference on High Performance Computing Simulation (HPCS)* (IEEE, Dublin, 2019), pp. 1051–1052.